

1 **Whistler wave interactions with superthermal electrons**  
2 **on Martian crustal magnetic fields: Bounce averaged**  
3 **diffusion coefficients and timescales**

4 **Alexander Shane<sup>1</sup> and Michael Liemohn<sup>1</sup>**

5 <sup>1</sup>Department of Climate and Space Sciences and Engineering, University of Michigan, Ann Arbor, MI,  
6 USA

7 **Key Points:**

- 8 • Low energy photoelectrons at Mars have fast wave-particle interaction timescales  
9 and can be scattered across the source cone.  
10 • High energy photoelectrons have slow wave-particle interaction timescales which  
11 restricts scattering across the source cone.  
12 • Trapped photoelectrons energized to high energies by whistler waves can then mod-  
13 ify the high energy distribution.

---

Corresponding author: Alexander Shane, [adshane@umich.edu](mailto:adshane@umich.edu)

This is the author manuscript accepted for publication and has undergone full peer review but has not been through the copyediting, typesetting, pagination and proofreading process, which may lead to differences between this version and the [Version of Record](#). Please cite this article as [doi: 10.1029/2021JA029118](https://doi.org/10.1029/2021JA029118).

This article is protected by copyright. All rights reserved.

14 **Abstract**

15 Pitch angle distributions of high energy superthermal electrons ( $>100$  eV) observed at  
 16 Mars show evidence of a ubiquitous energization process occurring on dayside crustal  
 17 magnetic fields. Wave-particle interactions have been put forth as one explanation and  
 18 in this study we investigate if the conditions are right at Mars for this process to occur  
 19 regularly. The resonant energy of electrons is not only dependent on the whistler wave  
 20 frequency and normal angle, but also the characteristic energy of the plasma environ-  
 21 ment. The characteristic energy is determined by the magnetic field strength and ther-  
 22 mal electron density, both measured quantities by the Mars Atmosphere and Volatile Evo-  
 23 lutionN mission. Bounce-averaged diffusion coefficients are calculated using a typical char-  
 24 acteristic energy profile and observed wave parameters. Time constants are also calcu-  
 25 lated and it is shown that wave-particle interactions are more efficient than Coulomb col-  
 26 lisions. Low energy electrons have fast wave-particle interaction timescales and electrons  
 27 can be scattered across the source cone and energized. High energy electrons have slow  
 28 wave-particle interactions timescales and electrons energized to these energies will be-  
 29 come trapped and modify the pitch angle distribution. Modeling the evolution of the elec-  
 30 tron distribution function will provide more insight into the process.

31 **1 Introduction**

32 Mars has a unique space environment relative to other planets in our solar system. The  
 33 Interplanetary Magnetic Field's (IMF) interaction with the ionosphere of Mars sets up  
 34 an induced magnetosphere, further complicated by the presence of localized crustal fields  
 35 that rotate with the planet. Superthermal electrons, electrons with energies ranging from  
 36 1-1000 eV, populate these crustal field lines during their time in the dayside hemisphere.  
 37 These electrons primarily consist of photoelectrons, produced from photoionization of  
 38 atmospheric neutrals, with peak production occurring around 130 km. Below the pho-  
 39 toelectron exobase, found to be  $\sim 150$  km by S. Xu et al. (2016), collisions dominate and  
 40 the electrons are lost locally. Above the photoelectron exobase, the particles are mag-  
 41 netized and can travel to high altitudes, eventually reaching the conjugate foot point of  
 42 the crustal magnetic field. The magnetic field strength decreases with altitude and the  
 43 electron's pitch angle becomes more field-aligned as it travels to higher altitudes due to  
 44 the conservation of the first adiabatic invariant. This source cone distribution is more  
 45 pronounced for higher energy electrons as Coulomb collisions are proportional to  $1/E^2$ ,  
 46 where  $E$  is the energy of the electron. Figure 1 of Shane et al. (2019) details this pitch  
 47 angle distribution (PAD) evolution along a field line as a function of energy.

48 Data from Mars Global Surveyor (MGS) and the Mars Atmosphere and Volatile Evo-  
 49 lutionN (MAVEN, (Jakosky et al., 2015)) mission have shown that our assumptions of the  
 50 PADs of superthermal electrons on the Martian crustal fields are incorrect, and that more  
 51 physics are involved than just collisions and single particle motion. Liemohn et al. (2003)  
 52 looked at a case study between MGS data and modeled electron fluxes and found that  
 53 MGS measured isotropic distributions for electrons with energies greater than 100 eV.  
 54 Brain et al. (2007) looked at the PADs of 115 eV electrons measured with MGS and showed  
 55 that isotropic and two-sided loss cones are the most common distributions on closed crustal  
 56 field lines. Shane et al. (2019) performed a statistical study using MAVEN data of su-  
 57 perthermal electron PADs on closed crustal field lines. They showed that electrons with  
 58 energies less than 60 eV have PADs that are in agreement with modeling results and that  
 59 adiabatic invariants and collisions describe the evolution of their distribution. Electrons  
 60 with energies greater than 60 eV were not in agreement and electrons with energies be-  
 61 tween 100-500 eV had a flux peak at perpendicular pitch angles. These results were two-  
 62 year averages and indicate that unstudied physics is occurring ubiquitously on crustal  
 63 fields.

Multiple explanations, including a magnetosheath source, were considered by Shane et al. (2019) and whistler mode waves were given as a probable mechanism for this flux peak at high energies as their interaction with electrons is energy dependent. Whistler waves are electromagnetic waves with frequencies between the lower hybrid frequency and the electron gyrofrequency. These waves are generated from a temperature anisotropy ( $T_{e,\perp} > T_{e,\parallel}$ ), where  $T_{e,\perp}$  and  $T_{e,\parallel}$  are the perpendicular and parallel electron temperature respectively, which was observed by Harada et al. (2016). They also saw most of their day-side wave events near the Magnetic Pileup Boundary, indicating that the waves or anisotropic electrons originated in the magnetosheath. Fowler et al. (2018) observed whistler wave generation as a byproduct of a magnetosonic wave event. The magnetosonic wave compresses the plasma, leading to a temperature anisotropy and wave growth. Fowler et al. (2020) looked at the same event but examined the effects of the whistler wave in greater detail. The waves were able to pitch angle scatter electrons, breaking their adiabaticity, and leading to parallel heating.

Quasi-linear theory is one method of analyzing wave-particle interactions which takes the Vlasov equation and separates variables into an average state and fluctuating state due to waves. This formulation of describing wave-particle interactions allows a presupposition of the wave variables (frequency and wave normal angle), and details the interaction with electrons using diffusion coefficients. Kennel and Engelmann (1966) gave the derivation of the quasi-linear diffusion equation and Lyons (1974a) transformed it into spherical coordinates (i.e. velocity and pitch angle). Lyons (1974b) then derived analytical expressions for whistler wave and ion cyclotron wave diffusion coefficients in an electron-proton plasma. More recently, Jordanova et al. (1996) investigated the effects of heavy ions on the diffusion coefficients.

In this study, we will characterize the background plasma conditions of the Mars environment using MAVEN measurements. The magnetic field strength and thermal electron density impact the energy of electrons resonant with a given whistler wave. We will use quasi-linear theory to calculate both local and bounce-averaged diffusion coefficients for Mars crustal field conditions. Few measurements of whistler waves have been observed at Mars, but we will use the observed wave parameters as inputs into our bounce-averaged calculations. Time constants of the wave-particle interaction will be calculated to estimate the efficiency of the interaction and compared to other relevant timescales such as the bounce period and Coulomb collision time constants.

## 2 Diffusion Coefficient Calculations

In this section we will describe the main equations and steps used to calculate the diffusion coefficients described by quasi-linear theory. The full details of the calculation and complete equation sets can be found in Lyons (1974b) and Jordanova et al. (1996). We note that these equations are non-relativistic and relativistic formulations can be found in Glauert and Horne (2005) and Albert (2005). Throughout this paper, we will be including the heavy ion effects from Jordanova et al. (1996). We will assume for this study that the ion composition of the upper Martian ionosphere contains 66%  $O^+$  and 34%  $O_2^+$ , corresponding to altitudes  $> 300$  km.

### 2.1 Resonant and Characteristic Energies

The resonance condition for wave-particle interactions is given in Equation (1) where  $v_{\parallel}$  is the parallel velocity of the particle relative to the local magnetic field,  $\omega_k$  is the wave frequency as a function of the wave vector  $\mathbf{k}$ ,  $\Omega = qB/m$  is the particle's cyclotron frequency,  $q$  is the particle's charge,  $B$  is the magnetic field strength,  $m$  is the particle's mass, and  $n$  is the harmonic, with Landau resonance given by  $n = 0$ .

$$v_{\parallel} = \frac{\omega_k}{k_{\parallel}} - \frac{n\Omega}{k_{\parallel}} \quad (1)$$

112 This equation states that the parallel velocity of the particle relative to the local mag-  
 113 netic field is equal to the parallel phase velocity of the wave. For harmonics  $|n| > 0$ ,  
 114 the wave frequency as seen by the particle is Doppler shifted by its parallel motion. Con-  
 115 sidering electrons as the resonant particle, waves where  $(\omega_{pe}/\Omega_e)^2 \gg \omega/\Omega_e$ , the reso-  
 116 nance condition (Equation 1), and the dispersion relation described by cold plasma the-  
 117 ory (Equation 7 in Lyons (1974b)), the parallel kinetic energy of particles resonant with  
 118 whistler waves can be calculated using Equation 2.

$$E_{\parallel, \text{res}} = E_c \frac{(1 + n\Omega_e/\omega_k)^2}{\cos^2 \theta} \Psi \quad (2)$$

119

$$E_c = \frac{B^2}{2\mu_0 n_e} \quad (3)$$

120 Here,  $\Omega_e$  no longer contains the sign of the charge (as well as for the remainder of this  
 121 paper), and  $\theta$  is the wave normal angle (the angle between the wave vector and the mag-  
 122 netic field).  $\Psi$  is a function of the wave normal angle and normalized wave frequency ( $\omega_k/\Omega$ ).  
 123 In the presence of heavy ions,  $\Psi$  is also a function of the fractional densities, mass ra-  
 124 tios, and charge numbers of each ion species (for brevity, we point the reader to Equa-  
 125 tions 8-12 in Jordanova et al. (1996)). The characteristic energy  $E_c$ , or available mag-  
 126 netic energy per particle, is given in Equation 3 and is strictly a function of the back-  
 127 ground magnetic field strength  $B$  and thermal electron density  $n_e$ . This means that the  
 128 energy of electrons resonant with a given whistler wave is dependent on the ambient plasma  
 129 conditions.

## 130 2.2 Diffusion Coefficients

131 The quasi-linear diffusion equation as given by Lyons (1974a) is:

$$\frac{\partial f}{\partial t} = \frac{1}{v \sin \alpha} \frac{\partial}{\partial \alpha} \left\{ \sin \alpha \left( D_{\alpha\alpha} \frac{1}{v} \frac{\partial f}{\partial \alpha} + D_{\alpha v} \frac{\partial f}{\partial v} \right) \right\} + \frac{1}{v^2} \frac{\partial}{\partial v} \left\{ v^2 \left( D_{v\alpha} \frac{1}{v} \frac{\partial f}{\partial \alpha} + D_{vv} \frac{\partial f}{\partial v} \right) \right\} \quad (4)$$

132 where  $f$  is the electron distribution function,  $\alpha$  and  $v$  are the electron's pitch angle and  
 133 velocity respectively, and the pitch angle, mixed, and velocity diffusion coefficients ( $D_{\alpha\alpha}$ ,  
 134  $D_{\alpha v}$ ,  $D_{vv}$ ) are given in (5).

$$\begin{aligned} D_{\alpha\alpha} &= \sum_{n=-\infty}^{\infty} \int_0^{x_{\max}} x D_{\alpha\alpha}^{nx} dx \\ D_{\alpha v} &= D_{v\alpha} = \sum_{n=-\infty}^{\infty} \int_0^{x_{\max}} x D_{\alpha v}^{nx} dx \\ D_{vv} &= \sum_{n=-\infty}^{\infty} \int_0^{x_{\max}} x D_{vv}^{nx} dx \end{aligned} \quad (5)$$

135 The diffusion coefficients need to be calculated as a function of harmonic  $n$  and wave nor-  
 136 mal angle  $\theta$ . They are then summed over each harmonic and integrated over  $x = \tan(\theta)$ .  
 137 In reality, only the pitch angle term needs to be calculated as the mixed and velocity terms  
 138 are related by:

$$\begin{aligned} D_{\alpha v}^{nx} &= D_{\alpha\alpha}^{nx} \left[ \frac{\sin \alpha \cos \alpha}{-\sin^2 \alpha - n\Omega/\omega_k} \right] \Big|_{\omega_k/\Omega=(\omega_k/\Omega)_{\text{res}}} \\ D_{vv}^{nx} &= D_{\alpha\alpha}^{nx} \left[ \frac{\sin \alpha \cos \alpha}{-\sin^2 \alpha - n\Omega/\omega_k} \right]^2 \Big|_{\omega_k/\Omega=(\omega_k/\Omega)_{\text{res}}} \end{aligned} \quad (6)$$

139 In order to calculate the diffusion coefficients, the frequency and wave normal angle dis-  
 140 tribution of the whistler waves must be specified. We use Gaussian distributions in both  
 141 frequency and  $x$  to describe such distributions in this study (Equations 7 and 8, respec-  
 142 tively).

$$B^2(\omega) = \begin{cases} B_0^2 \exp(-(\frac{\omega-\omega_m}{\delta\omega})^2) & \omega_{lc} \leq \omega \leq \omega_{uc} \\ 0 & \text{otherwise} \end{cases} \quad (7)$$

143

$$g(x) \propto \begin{cases} \exp\left(-\left(\frac{x-x_m}{\delta x}\right)^2\right) & x_{lc} \leq x \leq x_{uc} \\ 0 & \text{otherwise} \end{cases} \quad (8)$$

144

145

146

147

148

The variables needed to describe these distributions are the peaks  $(\omega_m, x_m)$ , the half widths  $(\delta\omega, \delta x)$ , the upper and lower cutoffs where waves do not exist outside of the given range  $(\omega_{lc}, \omega_{uc}, x_{lc}, x_{uc})$ , and the wave energy density,  $B_0^2$ . These distributions can be easily changed if observations indicate that these variables are not normally distributed. The final equation for the diffusion coefficient is as follows:

$$D_{\alpha\alpha}^{nx} = |\Omega| \frac{B_{wave}^2}{B^2} v^2 \pi^{\frac{1}{2}} \frac{\cos^5 \theta \left(\frac{\Omega}{\delta\omega}\right) \left(-\sin^2 \alpha - \frac{n\Omega}{\omega_k}\right)^2}{\Psi^{\frac{3}{2}} \left|1 + \frac{n\Omega}{\omega_k}\right|^3 I(\omega_k)} |\Theta_{n,k}|^2 \times \frac{\exp\left[-\frac{(\omega_k - \omega_m)^2}{\delta\omega^2} - \frac{(x - x_m)^2}{\delta x^2}\right]}{\text{erf}\left[\frac{\omega_{uc} - \omega_m}{\delta\omega}\right] + \text{erf}\left[\frac{\omega_m - \omega_{lc}}{\delta\omega}\right]} \left(1 - \frac{1}{v_{\parallel}} \frac{\delta\omega_k}{\delta k_{\parallel}} \Big|_x\right)^{-1} \Big|_{\omega_k/\Omega = (\omega_k/\Omega)_{res}} \quad (9)$$

149

150

151

152

153

154

155

In Equation (9),  $B_{wave}^2$  is the total wave amplitude and can be computed from Equation (7).  $|\Theta_{n,k}|$ ,  $I(\omega_k)$ , and  $\left(1 - \frac{1}{v_{\parallel}} \frac{\delta\omega_k}{\delta k_{\parallel}}\right)$  are all functions of the wave parameters and the latter two are modified by the presence of heavy ions. We point the reader to Lyons (1974b) and Jordanova et al. (1996) for full details on this derivation. In order to calculate the diffusion coefficients as a function of energy and pitch angle for a given whistler wave distribution (number of harmonics, frequency, wave normal angle, and  $B_{wave}$ ) the steps are as follows:

156

157

158

159

160

161

162

163

164

165

1. Calculate the characteristic energy ( $E_c$ ) from the magnetic field strength and thermal electron density
2. For each harmonic/wave normal angle combination, determine the parallel resonant energies as a function of wave frequency (Equation 2)
3. For each energy, determine which pitch angles the parallel resonant energies correspond to
4. Calculate diffusion coefficients for each resonant frequency as a function of pitch angle, wave normal angle, and harmonic
5. Integrate over wave normal angle range
6. Sum over specified harmonics

166

167

168

169

The resultant diffusion coefficient distribution in energy-pitch angle space have units of  $cm^2 s^{-3}$ . However, these are local coefficients and bounce-averaged diffusion coefficients give a more complete description of the wave-particle interaction as an electron travels along a field line.

170

### 2.3 Bounce Averaging

171

172

173

174

175

176

177

178

179

180

181

182

The local diffusion coefficients only give information about the wave-particle interaction at a single location, but the electrons and the wave are traveling along the magnetic field line. The energy and local pitch angle of an electron dictates how fast it travels through any given region, and the pitch angle changes with varying magnetic field strength. The characteristic energy and normalized wave frequency will also change, shifting the diffusion coefficient distribution in energy-local pitch angle space. Bounce-averaged diffusion coefficients take into account these changes and provide an aggregate description of the wave-particle interaction (e.g., Lyons et al., 1972; Zhao et al., 2015). The equations are given in Equation 10, where  $\alpha_{eq}$  is the equatorial pitch angle of the electron and the superscript *ba* denotes bounce-averaged.  $\tau_b$  is the bounce period of an electron and is given in Equation 11. Here we are assuming a symmetric dipole field line where  $s_1$  and  $s_2$  are the mirror point and top of the field line, respectively. The integral is over

183 a quarter-bounce and therefore a factor of 4 is needed.

$$D_{\alpha\alpha}^{ba}(E, \alpha_{eq}) = \frac{4}{\tau_b(E, \alpha_{eq}) v} \int_{s_1}^{s_2} D_{\alpha\alpha}(E, \alpha) \left(\frac{\partial \alpha_{eq}}{\partial \alpha}\right)^2 \frac{ds}{\cos \alpha} \quad (10)$$

$$D_{EE}^{ba}(E, \alpha_{eq}) = \frac{4}{\tau_b(E, \alpha_{eq}) v} \int_{s_1}^{s_2} D_{EE}(E, \alpha) \frac{ds}{\cos \alpha}$$

$$\tau_b(E, \alpha_{eq}) = \frac{4}{v} \int_{s_1}^{s_2} \frac{ds}{\cos \alpha} \quad (11)$$

### 184 3 Characteristic Energies Observed by MAVEN

185 The resonant energy and pitch angle of superthermal electrons with a given wave is de-  
 186 termined by the frequency and wave normal angle of the wave. The characteristic en-  
 187 ergy is a multiplicative scaling factor determined by the local magnetic field strength and  
 188 thermal electron density. These are both quantities measured by MAVEN and the char-  
 189 acteristic energy distribution of the Martian space environment can be quantified and  
 190 used to construct representative altitude profiles for calculating bounce-averaged diffu-  
 191 sion coefficients.

192 We use data from the Magnetometer (MAG, Connerney et al. (2015)) and the Langmuir  
 193 Probes and Waves (LPW, Andersson et al. (2015)) instruments to analyze the charac-  
 194 teristic energies observed in the Martian space environment. We use the same criteria  
 195 as Shane et al. (2019) to filter for dayside crustal fields for continuity between the pitch  
 196 angle distributions and the characteristic energies measured. The solar zenith angle must  
 197 be less than  $90^\circ$  to ensure dayside observations. All observations are at altitudes greater  
 198 than 200 km so that our measurement is above the photoelectron exobase and the elec-  
 199 trons are magnetized. The shape parameter (S. Xu et al., 2017) is used to determine that  
 200 photoelectrons are in the source cone. This looks at the energy spectrum of 20-80 eV elec-  
 201 trons at field aligned pitch angles and determines a goodness of fit to a typical photo-  
 202 electron spectra. A magnetic field minimum of 20 nT is used so that we exclude deeply  
 203 draped fields and a spacecraft potential filter is also set.

204 Figure 1 plots the combined 2d histogram of magnetic field strength and thermal elec-  
 205 tron density observed with MAVEN on dayside crustal fields. The histograms for each  
 206 individual quantity are plotted on the right and top left subplots. We mask any bin with  
 207 sample size  $< 10$  and the maximum sample size in a bin is 2500. Overlaid on the 2d his-  
 208 togram are characteristic energy contours. In the upper right of the figure is a histogram  
 209 of all characteristic energies observed. This value spans orders of magnitude with the ma-  
 210 jority of observations between  $E_c = 0.1-100$  eV. Some studies use the value  $f_{pe}/f_{ce} =$   
 211  $(E_c/m_e c^2)^{-\frac{1}{2}}$ , the ratio of the plasma to electron cyclotron frequency, instead. Charac-  
 212 teristic energies of 0.1, 1, 100, and 1000 eV correspond to  $f_{pe}/f_{ce} = 2262.3, 715.4, 226.2,$   
 213 and 71.5, respectively.

214 Figure 2 further explores the characteristic energy distribution at Mars by plotting the  
 215 median value against (a) altitude, (b) local time, and (c) magnetic elevation angle. The  
 216 magnetic elevation angle is defined to be  $0^\circ$  when parallel with the surface, and  $90^\circ$  when  
 217 perpendicular. The region between the 25th and 75th percentiles is shaded. The geo-  
 218 metric mean lies on top of the median and the arithmetic mean is much greater than the  
 219 75th percentile, highlighting the lognormal distribution of the characteristic energy. The  
 220 altitude profile shows that the characteristic energy is likely to be greater at higher al-  
 221 titudes. While both the magnetic field and electron density typically decrease with al-  
 222 titude, the electron density can vary over orders of magnitude, dominating the net change  
 223 to the characteristic energy. There is little to no dependence on local time and magnetic

224 elevation angle. However the characteristic energy on vertical field lines has a longer tail  
 225 to the distribution.

#### 226 4 Local Diffusion Coefficients Distribution

227 In Figure 3 we show local pitch angle (top row) and energy (bottom row) diffusion co-  
 228 efficient distributions for two characteristic energies: 30 eV (left column) and 100 eV (right  
 229 column). The whistlers observed by Harada et al. (2016) were on the order of  $0.1\Omega_e$  prop-  
 230 agating quasi-parallel to the magnetic field. Those observed by Fowler et al. (2020) were  
 231 between  $0.1-0.5\Omega_e$  and while they could not estimate the wave normal angle, at these  
 232 frequencies the resonance cone limits wave propagation at angles higher than  $\sim 60^\circ$ . In  
 233 this study, we will use a wave frequency distribution that ranges from  $\omega_{lc} = 0.1\Omega_e$  to  
 234  $\omega_{uc} = 0.5\Omega_e$ , with the peak at  $\omega_m = 0.25\Omega_e$ , and the width  $\delta\omega = 0.25\Omega_e$ . The wave  
 235 normal angle distribution is assumed to be quasi-parallel from  $\theta_{lc} = 0^\circ$  to  $\theta_{uc} = 45^\circ$ ,  
 236 peaked at  $\theta_m = 0^\circ$  and width  $\delta\theta = 45^\circ$ . The value of the wave energy density,  $B_0^2$ , is  
 237 taken from Harada et al. (2016). The values observed in their study were between  $10^{-4}$   
 238 and  $10^{-2}$  nT<sup>2</sup>/Hz and we use a conservative low value of  $10^{-4}$  nT<sup>2</sup>/Hz here. Only Lan-  
 239 dau resonance ( $n = 0$ ) is shown in Figure 3. The shape of these distributions traces the  
 240 curve defined by  $E_{\text{res}} = E_{\parallel, \text{res}} / \cos^2(\alpha)$  and the white space denotes areas where wave-  
 241 particle interactions do not occur for the specified wave in the chosen characteristic en-  
 242 ergy environment. For harmonics  $|n| \geq 0$ , the diffusion coefficient distribution will be  
 243 a superposition of each harmonic resonant energy curve.

244 Other wave parameters were investigated and results are described here. An increase to  
 245 the characteristic energy shifts the entire diffusion coefficient distribution to higher en-  
 246 ergies, while a decrease in characteristic energy shifts the distribution to lower energies.  
 247 Decreasing the width of the Gaussian in frequency to  $\delta\omega = 0.1\Omega_e$  decreases the mag-  
 248 nitude of the diffusion coefficients for all energies and pitch angles and increasing the width  
 249 to  $\delta\omega = 0.5\Omega_e$  increases the magnitude of the diffusion coefficients. Shifting the peak  
 250 of the wave frequency Gaussian puts more wave power into those frequencies near the  
 251 peak. A shift of the peak to the lower cutoff frequency increases the magnitude of the  
 252 diffusion coefficients of those electrons resonant with the lower frequencies, i.e. the lower  
 253 energy resonant curves of the diffusion coefficient distribution. The diffusion coefficients  
 254 along the higher energy resonant curves are decreased. The opposite is true if the fre-  
 255 quency peak is moved to the upper cutoff frequency. In this case, the magnitude of the  
 256 diffusion coefficients are increased along the higher energy resonant curves and the dif-  
 257 fusion coefficients along the lower energy resonant curves are decreased. Quantifying the  
 258 exact energies of the resonant curves which see an increase or decrease to the diffusion  
 259 coefficients along them is determined by where the two Gaussians in resonant frequency  
 260 intersect. The combination of  $\frac{\Psi}{\cos^2\theta}$  in Equation 2 results in field aligned whistler waves  
 261 contributing to the entire diffusion coefficient distribution. The more oblique the wave  
 262 normal angle is the less it contributes to the lower energy resonant curves. Therefore shift-  
 263 ing the peak of the Gaussian in wave normal angle to more oblique wave normal angles  
 264 increases the magnitude of the diffusion coefficients along higher energy resonant curves  
 265 and decreases the magnitude along the lower energy curves. Halving the Gaussian width  
 266 in wave normal angle puts less wave power into more oblique waves and therefore this  
 267 has the opposite effect as shifting the peak. The changes made to the Gaussian param-  
 268 eters in frequency and wave normal angle only have the affect of altering along which  
 269 corresponding  $E_{\parallel, \text{res}}$  curves will have a higher or lower diffusion coefficient magnitude.  
 270 As long as the upper and lower cutoffs are held constant, the shape and area of the dif-  
 271 fusion coefficient distribution will also remain constant.

## 5 Bounce-Averaged Diffusion Coefficients

The motion of both electrons and the whistler wave along the field line makes interpretation of local diffusion coefficients limited. Bounce-averaging takes into account the change in pitch angle of the electron, the time the electron spends in any given region along the magnetic field, the local characteristic energy, and the change in normalized wave frequency as the local gyrofrequency is shifted due to the change in magnetic field strength. In this section, we perform three runs of an idealized bounce-averaging model on a Martian crustal field line. The three runs differ by the characteristic energy profile used along the field line.

### 5.1 Methodology

Some background parameters for our bounce-averaged runs are shown in Figure 4. Using the dipole field equations, we set up an idealized crustal field. Given a minimum and maximum magnetic field strength and the vertical distance between the two values, a dipole field can be constructed. The field extends from the exobase at 160 km where the field strength is  $\sim 294$  nT to the top of the crustal field at 500 km with a field strength of 50 nT. A thermal electron density profile is taken from MGITM (Bougher et al., 2015) and the log of the density is linearly interpolated above 250 km. For Run 1, we increase the thermal electron density profile by a factor of 5 to reproduce the geometric mean/median characteristic energy distribution observed by MAVEN. No change is made for Run 2 and the resulting characteristic energy distribution is representative of the arithmetic mean measured by MAVEN. For direct comparison, these MAVEN profiles are plotted again in Figure 4. Lastly, we divide the electron density profile by a factor of 5 for Run 3. This is to investigate the wave-particle interactions at high characteristic energies, which causes less interaction with low energy electrons. Above 300 km, we use the rough assumption that the ion composition consists of 66%  $O^+$  and 34%  $O_2^+$ , and for altitudes below 300 km the ion composition is made up of 90%  $O_2^+$  and 10%  $CO_2^+$ . We note that the addition of heavy ions have little effect on the calculations because the assumed wave frequencies are much greater than the ion gyrofrequencies. The normalized frequency and wave normal angle distribution of the whistler wave are identical to those in Figure 3 and the frequency is unnormalized by the gyrofrequency at the top of the field line. The normalized frequency of the wave is then dependent on the location along the magnetic field, and the actual frequency of the wave (in Hz) remains constant. No effort is made to model the change in wave normal angle as the wave propagates and the wave is assumed to exist at all locations along the field line. For the bounce-averaged runs, we include harmonics  $|n| \leq 3$ , as these higher harmonics will affect the energies of interest. Although the crustal fields are not symmetric about the Martian equator, we will still use the term “equatorial pitch angle” to indicate the minimum-B pitch angle.

Care is needed around the bounce location to achieve convergence. This is accomplished by defining a refinement region where the magnetic field grid has a higher resolution. The magnetic field strengths where the electron’s local pitch angle is between  $89^\circ$  and  $90^\circ$  defines this region and is different depending on the equatorial pitch angle of the electron. We found that using 1000 grid points to define the magnetic field, with a third of them used in the refinement region, is sufficient to achieve convergence of the bounce integrals.

The foot points of the dayside crustal fields are embedded in the ionosphere and so there is a constant source of electrons at field aligned pitch angles. These electrons stream from one foot point to the other and likely deposit their energy on the conjugate side. Some of these electrons will be pitch angle scattered so their mirror point is at a higher altitude than the photoelectron exobase. We calculate bounce-averaged diffusion coefficients for both populations, the source cone and the trapped electrons. In these calculations we assume all source cone electrons are lost upon reaching the conjugate ionosphere, and



thus the integral is only over half a bounce period. It is important to note that the source cone electrons are thought to be the main population of electrons on closed crustal fields and should be included in these calculations.

Figure 5 shows the pitch angle trajectories through altitude and local pitch angle space given multiple equatorial pitch angles. The third run conditions are used here. The color is the magnitude of the diffusion coefficients and graphically depicts where wave-particle interactions occur in altitude for 25 eV electrons. While the pitch angle trajectories are independent of energy, the diffusion coefficient distribution will vary. A 25 eV electron with an equatorial pitch angle of  $60^\circ$  will have little interaction with the specified wave during its bounce period, while the  $40^\circ$  electron will be in resonance with the wave for the majority of its bounce. An electron on the edge of the source cone ( $24.33^\circ$ ) will not be in a wave-particle interaction region for most altitudes but is in resonance near its bounce, where the most time is spent. This figure highlights the necessity to calculate the bounce-averaged coefficients as opposed to looking at a single location along the field line.

It is useful to consider the relative importance of wave-particle interactions against other processes influencing the superthermal electron distribution on Mars crustal field lines. Above the exobase, although electrons are considered magnetized, Coulomb collisions still have an influence on the pitch angle distributions, especially at lower energies. A comparison of the timescales of wave-particle interactions to the Coulomb collision timescale will provide insight into the effectiveness of the pitch angle scattering and energization of superthermal electrons due to waves. Order-of-magnitude estimates of the time constants of wave-particle interactions have been calculated as

$$\tau = v^2/D \quad (12)$$

which arises from dimensional analysis of Equation 4 (e.g., Lyons, 1974a; Liemohn et al., 1997). This is a rough estimate that completely ignores variations in  $D$  or  $f$  but yields an order of magnitude value that can be assessed for effectiveness. Coulomb collisions timescales can be calculated as

$$\tau_{cc} = \frac{\beta^4 v^3}{2An_e} \quad (13)$$

where  $\beta = 1.7 \times 10^{-8} \sqrt{eV} \text{ s cm}^{-1}$ ,  $A = 2.6 \times 10^{-12} eV^2 \text{ cm}^2$ ,  $v$  is the electron's velocity, and  $n_e$  is the thermal electron density (Liemohn et al., 1997). These quantities can be calculated using bounce averaged diffusion coefficients and thermal electron density and will be compared to determine the relative effectiveness of the wave-particle interactions.

## 5.2 Results

Figure 6 plots the bounce-averaged diffusion coefficients for Runs 1, 2 and 3 (left, middle and right columns, respectively). The top row plots the pitch angle diffusion coefficients and the bottom row plots the energy diffusion coefficients. The source cone pitch angle is denoted by a black dashed line. The shift of the diffusion coefficient distribution to higher energies due to the higher characteristic energy profiles used from Run 1 to Run 3. Resonant energy curves can be seen and this comes from the superposition of the harmonics. For the majority of velocity space, the pitch angle diffusion coefficients are greater than the energy diffusion coefficients.

To assess the effectiveness of the wave-particle interaction along the crustal magnetic field, time constants can be estimated via Equation 12 and compared against Coulomb collision timescales. These time constants are shown in Figure 7. The columns from left to right are for Runs 1, 2, and 3, respectively. The top row plots the pitch angle scattering timescale, the middle row plots the energization timescale, and the bottom row plots the Coulomb collision timescale. The color scale has been chosen such that the color fades

370 to white around 1 hour, highlighting the regions of velocity space with fast timescales  
 371 for each process. MAVEN data shows that the high energy perpendicular peak can be  
 372 seen by 7 LT, indicating the process responsible happens on sub-hour timescales. For  
 373 reference, bounce periods on this crustal field for these energies are between 0.1-1.5 sec-  
 374 onds.

375 Figure 8 compares the multiple timescales of interest against each other. Again, the columns  
 376 from left to right are for Runs 1, 2, and 3, respectively and the black dashed line denotes  
 377 the source cone pitch angle. Each row has a different color bar, but each color bar di-  
 378 verges at a value of 1. The top row plots the ratio of the fastest wave-particle interac-  
 379 tion timescale to the bounce period. Blue regions indicate where the wave-particle in-  
 380 teraction timescale is sub-bounce. The middle row plots the ratio of the pitch angle scat-  
 381 tering timescale to energization timescale. Blue regions indicate where pitch angle scat-  
 382 tering is faster process than energization. Lastly, the bottom row plots the ratio of the  
 383 fastest wave-particle interaction timescale to the Coulomb collision timescale. Blue re-  
 384 gions indicate where wave-particle interactions are faster than Coulomb collision scat-  
 385 tering.

386 Figure 5 showed that electrons with different pitch angles and energies will interact with  
 387 the prescribed whistler wave at different altitudes. We have used the logarithm base 10  
 388 of the diffusion coefficients as weights to quantify the weighted average altitude of wave-  
 389 particle interactions. Figure 9 shows these results and the columns from left to right are  
 390 for Runs 1-3, respectively. The strongest interaction between whistler wave and parti-  
 391 cle occurs near the top of the field line for the trapped electrons. Source cone electrons  
 392 generally have their strongest interaction at slightly lower altitudes than the trapped elec-  
 393 trons but closer to the top of the field line than the exobase altitude.

## 394 6 Discussion and Conclusions

395 Several key factors of electron interactions with whistler mode waves have been presented  
 396 above. We have covered characteristic energies, diffusion coefficients, and order-of-magnitude  
 397 time constant estimates. We also discussed the limitations of interpreting local wave-particle  
 398 interactions and modeled bounce-averaged quantities along idealized Martian crustal mag-  
 399 netic fields. Here, we recap those results and interpret them with respect to the relative  
 400 effectiveness of these waves influencing the velocity space distribution of superthermal  
 401 electrons on crustal field lines at Mars.

402 From data taken by the MAG and LPW instruments aboard MAVEN, the character-  
 403 istic energy of the environment can be calculated. This quantity appears in the equa-  
 404 tion for the energy of electrons resonant with a particular whistler wave. Determining  
 405 the typical range of values of this quantity at Mars will help us create idealized altitude  
 406 profiles to calculate bounce-averaged diffusion coefficients. The majority of magnetic field  
 407 and plasma density values observed yield characteristic energy values between 0.1 and  
 408 100 eV ( $f_{pe}/f_{ce} = 2261$  and 715), with the peak of the distribution between 1 and 10  
 409 eV ( $f_{pe}/f_{ce} = 715$  and 71). The altitude distribution of the characteristic energy shows  
 410 that at higher altitudes, the characteristic energy is likely to be higher. While for any  
 411 given crustal magnetic field, the field strength decreases with altitude, the correspond-  
 412 ing decrease to the characteristic energy is likely offset by the orders of magnitude de-  
 413 crease in the electron density. The tail of the characteristic energy distribution gets longer  
 414 with increasing altitude, indicated by the larger mean-to-median ratios and the spread  
 415 of the quartiles at higher altitudes. This high energy tail also exists for vertical magnetic  
 416 fields. Vertical fields are measured more at low altitudes, where the characteristic en-  
 417 ergies are lower, so the larger spread in the data is possibly due to low sampling of ver-  
 418 tical fields in our dataset. There is little-to-no variation in the median characteristic en-  
 419 ergy as a function of local time. No variations were seen in the electron pitch angle dis-  
 420 tributions as a function of local time (Shane et al., 2019), and the little variation in the

421 characteristic energy distribution with respect to local time helps support the hypoth-  
 422 esis that wave-particle interactions cause the observed superthermal electron velocity space  
 423 distribution on Mars crustal field lines.

424 Our idealized modeling of bounce-averaged diffusion coefficients reveal the complex nature  
 425 of wave-particle interactions when the particle's trajectory and changing plasma environ-  
 426 ment is taken into account. We used characteristic energy profiles that match the  
 427 typical Martian space environment as observed by MAVEN and our wave parameters  
 428 are based off the observations of Harada et al. (2016) and Fowler et al. (2020). We note  
 429 again that the wave parameters probably change as the wave propagates along the mag-  
 430 netic field and our assumption that the wave is omnipresent may be false for any given  
 431 scenario. If whistlers are common on crustal fields, the waves are likely to be of mag-  
 432 netosheath origin, where the temperature anisotropy of the superthermal electrons leads  
 433 to wave growth (Harada et al., 2016). A ray tracing model can determine if these waves  
 434 can propagate across draped fields and onto crustal fields. Furthermore, the reflection  
 435 of these waves could also give insight into where wave-particle interactions are allowed.  
 436 Whistler waves have been shown to be reflected when the wave frequency approaches the  
 437 local lower hybrid frequency (e.g., Kuzichev & Shklyar, 2013; X. Xu et al., 2020). Our  
 438 idealized scenarios had the strongest wave-particle interactions at high altitudes. If there  
 439 is lower altitude reflection or absorption point, strong wave-particle interactions will still  
 440 occur.

441 Runs 1 and 2 have characteristic energy profiles most representative of the average Mar-  
 442 tian space environment. In both these scenarios, the timescales of the wave-particle in-  
 443 teraction are generally greater than a bounce period. Sub-bounce wave-particle inter-  
 444 actions will happen for low energy electrons ( $< 20$  eV for Run 1 and  $< 50$  eV for Run  
 445 2). In both of these regions of velocity space, pitch angle scattering will be a fast pro-  
 446 cess. Once the distribution is sufficiently isotropized, efficient energization can occur. While  
 447 Shane et al. (2019) did observe source cone distributions for electrons with  $E < 60$  eV,  
 448 the ratio of the field-aligned to perpendicular pitch angles was actually quite low com-  
 449 pared to modeling results. The fast timescales of interaction near the source cone bound-  
 450 ary allows for the trapped and source cone electron populations to mix while keeping the  
 451 source cone shape, since there is always a steady source in the dayside ionosphere. At  
 452 higher energies, the timescales of wave-particle interaction become much longer than a  
 453 bounce period and the long timescales at the source cone boundary indicates the source  
 454 cone and trapped electron populations are unable to mix sufficiently well, and any change  
 455 to the trapped electron distribution will have an effect on the PAD. Low energy electrons  
 456 pitch angle scattered to perpendicular pitch angles and then energized could have an ap-  
 457 preciable effect on the high energy PAD, especially given the orders of magnitude dif-  
 458 ference in flux. These two runs imply that wave-particle interactions could produce the  
 459 observed distributions. In Run 1, the source cone timescales become large compared to  
 460 a bounce period around 50 eV, near the energy limit where Shane et al. (2019) saw the  
 461 change from source cone distribution to trapped distribution. The strongest interactions  
 462 occur at high altitudes, allowing for particles to be trapped more easily. In Run 3, the  
 463 wave-particle interaction timescales are fairly uniform with respect to energy above 30  
 464 eV. The lack of energy dependence does not match with MAVEN observations. In all  
 465 runs, the wave-particle interactions happens on timescales shorter than Coulomb colli-  
 466 sions (except for high energy source cone electrons in Run 1 and low energy electrons  
 467 in Run 3). This occurs even though we change the electron density profile between the  
 468 three runs, indicating that whistler waves are the dominant process controlling the elec-  
 469 tron distribution function if present.

470 The pitch angle distributions of high energy electrons observed by both MGS (Liemohn  
 471 et al., 2003; Brain et al., 2007) and MAVEN (Shane et al., 2019) suggest that unstud-  
 472 ied physics are occurring regularly at Mars. In this study, we have investigated the fea-  
 473 sibility of whistler waves as the proposed mechanism. The distribution of the character-

474 istic energy on the dayside crustal magnetic fields has been analyzed using MAVEN data.  
 475 With the average altitude distributions and using the observed wave parameters by Harada  
 476 et al. (2016) and Fowler et al. (2020), we analyzed the bounce-averaged diffusion coef-  
 477 ficients, timescales of the interaction, and altitude at which the strongest wave-particle  
 478 interaction occurs. The results indicate that wave-particle interactions are more impor-  
 479 tant than Coulomb collisions above the exobase. Runs 1 and 2 showed that the wave par-  
 480 ticle interaction process is slow at low energies and allows for mixing between the source  
 481 cone and trapped population. This could be why the source cone distributions seen at  
 482 low energies by MAVEN have a low ratio between the parallel and trapped flux. Fur-  
 483 thermore, these scenarios had long timescales of interaction at high energies, restricting  
 484 mixing between the two populations. If there is energization from low to high energies,  
 485 these electrons are now trapped and this scenario may produce the observed PADs. The  
 486 flux of electrons at low energies is orders of magnitude larger than the flux at high en-  
 487 ergies, so only a small fraction of low energy electrons need to be energized to produce  
 488 the observed distribution. While time constants can help gauge importance of terms in  
 489 relation to each other and help determine the efficiency of the process, they cannot give  
 490 sufficient information about the resulting electron distribution. Modeling of the bounce-  
 491 averaged quasi-linear diffusion equation is essential for understanding the evolution of  
 492 electron velocity space distribution due to wave-particle interactions.

### 493 Acknowledgments

494 This work was supported by the National Aeronautics and Space Administration (NASA)  
 495 Grant NNX16AQ04G to the University of Michigan. The MAVEN project is funded by  
 496 NASA through the Mars Exploration Program. All MAVEN data can be accessed through  
 497 the Planetary Data System (<https://pds.nasa.gov/>). The filtered pitch angle distribu-  
 498 tion dataset can be found at <https://doi.org/10.7302/ya0j-kh60>.

### 499 References

- 500 Albert, J. M. (2005). Evaluation of quasi-linear diffusion coefficients for whistler  
 501 mode waves in a plasma with arbitrary density ratio. *Journal of Geophysical*  
 502 *Research: Space Physics*, *110*(A3). doi: 10.1029/2004JA010844
- 503 Andersson, L., Ergun, R. E., Delory, G. T., Eriksson, A., Westfall, J., Reed,  
 504 H., ... Meyers, D. (2015). The Langmuir Probe and Waves (LPW) In-  
 505 strument for MAVEN. *Space Science Reviews*, *195*(1), 173–198. doi:  
 506 10.1007/s11214-015-0194-3
- 507 Bougher, S. W., Pawlowski, D., Bell, J. M., Nelli, S., McDunn, T., Murphy, J. R.,  
 508 ... Ridley, A. (2015). Mars global ionosphere-thermosphere model: Solar cy-  
 509 cle, seasonal, and diurnal variations of the mars upper atmosphere. *Journal of*  
 510 *Geophysical Research: Planets*, *120*(2), 311–342. doi: 10.1002/2014JE004715
- 511 Brain, D., Lillis, R. J., Mitchell, D. L., Halekas, J. S., & Lin, R. P. (2007). Electron  
 512 pitch angle distributions as indicators of magnetic field topology near Mars. *J.*  
 513 *Geophys. Res.*, *112*(A9), A09201–A09201. doi: 10.1029/2007JA012435
- 514 Connerney, J. E. P., Espley, J., Lawton, P., Murphy, S., Odom, J., Oliverson, R., &  
 515 Sheppard, D. (2015, dec). The MAVEN Magnetic Field Investigation. *Space*  
 516 *Science Reviews*, *195*(1), 257–291. doi: 10.1007/s11214-015-0169-4
- 517 Fowler, C. M., Agapitov, O. V., Xu, S., Mitchell, D. L., Andersson, L., Artemyev,  
 518 A., ... Mazelle, C. (2020). Localized heating of the martian topside ionosphere  
 519 through the combined effects of magnetic pumping by large-scale magnetosonic  
 520 waves and pitch angle diffusion by whistler waves. *Geophysical Research Let-*  
 521 *ters*, *47*(5). doi: 10.1029/2019GL086408
- 522 Fowler, C. M., Andersson, L., Ergun, R. E., Harada, Y., Hara, T., Collinson, G., ...  
 523 Jakosky, B. M. (2018). MAVEN Observations of Solar Wind-Driven Magne-  
 524 tosonic Waves Heating the Martian Dayside Ionosphere. *Journal of Geophysi-*

- 525 *cal Research: Space Physics*, 123(5), 4129–4149. doi: 10.1029/2018JA025208
- 526 Glauert, S. A., & Horne, R. B. (2005). Calculation of pitch angle and energy diffu-  
527 sion coefficients with the PADIE code. *Journal of Geophysical Research: Space*  
528 *Physics*, 110(A4). doi: <https://doi.org/10.1029/2004JA010851>
- 529 Harada, Y., Andersson, L., Fowler, C. M., Mitchell, D. L., Halekas, J. S., Mazelle,  
530 C., ... Jakosky, B. M. (2016). Maven observations of electron-induced whistler  
531 mode waves in the martian magnetosphere. *Journal of Geophysical Research:*  
532 *Space Physics*, 121(10), 9717–9731. doi: 10.1002/2016JA023194
- 533 Jakosky, B. M., Lin, R. P., Grebowsky, J. M., Luhmann, J. G., Mitchell, D. F.,  
534 Beutelschies, G., ... Zurek, R. (2015). The mars atmosphere and volatile  
535 evolution (maven) mission. *Space Science Reviews*, 195(1), 3–48. doi:  
536 10.1007/s11214-015-0139-x
- 537 Jordanova, V. K., Kozyra, J. U., & Nagy, A. F. (1996). Effects of heavy ions on the  
538 quasi-linear diffusion coefficients from resonant interactions with electromag-  
539 netic ion cyclotron waves. *Journal of Geophysical Research: Space Physics*,  
540 101(A9), 19771–19778. doi: 10.1029/96JA01641
- 541 Kennel, C. F., & Engelmann, F. (1966, 2020/03/11). Velocity space diffusion from  
542 weak plasma turbulence in a magnetic field. *The Physics of Fluids*, 9(12),  
543 2377–2388. doi: 10.1063/1.1761629
- 544 Kuzichev, I. V., & Shklyar, D. R. (2013). Full-wave description of the lower hybrid  
545 reflection of whistler waves. *Plasma Physics Reports*, 39(10), 795–808. doi: 10  
546 .1134/S1063780X13090043
- 547 Liemohn, M. W., Khazanov, G. V., & U., K. J. (1997). Guided plasmaspheric hiss  
548 interactions with superthermal electrons 1. Resonance curves and timescales.  
549 *Journal of Geophysical Research A: Space Physics*, 102(6), 11619–11623. doi:  
550 10.1029/97JA00825
- 551 Liemohn, M. W., Mitchell, D. L., Nagy, A. F., Fox, J. L., Reimer, T. W., & Ma,  
552 Y. (2003). Comparisons of electron fluxes measured in the crustal fields at  
553 Mars by the MGS magnetometer/electron reflectometer instrument with a B  
554 field-dependent transport code. *Journal of Geophysical Research: Planets*,  
555 108(E12). doi: doi:10.1029/2003JE002158
- 556 Lyons, L. R. (1974a). General relations for resonant particle diffusion in  
557 pitch angle and energy. *J. Plasma Physics*, 12(1), 45–49. doi: 10.1017/  
558 S0022377800024910
- 559 Lyons, L. R. (1974b). Pitch angle and energy diffusion coefficients from resonant  
560 interactions with ion–cyclotron and whistler waves. *J. Plasma Physics*, 12(3),  
561 417–432. doi: DOI:10.1017/S002237780002537X
- 562 Lyons, L. R., Thorne, R. M., & Kennel, C. F. (1972, 2020/08/18). Pitch-angle dif-  
563 fusion of radiation belt electrons within the plasmasphere. *Journal of Geophys-*  
564 *ical Research (1896-1977)*, 77(19), 3455–3474. doi: 10.1029/JA077i019p03455
- 565 Shane, A., Liemohn, M., Florie, C., & Xu, S. (2019, 2020/06/17). Misbehaving  
566 high-energy electrons: Evidence in support of ubiquitous wave-particle interac-  
567 tions on dayside martian closed crustal magnetic fields. *Geophysical Research*  
568 *Letters*, 46(21), 11689–11697. doi: 10.1029/2019GL084919
- 569 Xu, S., Liemohn, M., Bougher, S., & Mitchell, D. (2016, 2020/07/28). Martian high-  
570 altitude photoelectrons independent of solar zenith angle. *Journal of Geophys-*  
571 *ical Research: Space Physics*, 121(4), 3767–3780. doi: 10.1002/2015JA022149
- 572 Xu, S., Mitchell, D., Liemohn, M., Fang, X., Ma, Y., Luhmann, J., ... Jakosky, B.  
573 (2017, 2020/07/28). Martian low-altitude magnetic topology deduced from  
574 maven/swea observations. *Journal of Geophysical Research: Space Physics*,  
575 122(2), 1831–1852. doi: 10.1002/2016JA023467
- 576 Xu, X., Chen, L., Zhou, C., Liu, X., Xia, Z., Simpson, J. J., & Zhang, Y. (2020,  
577 2020/07/28). Two-dimensional full-wave simulation of whistler mode wave  
578 propagation near the local lower hybrid resonance frequency in a dipole field.  
579 *Journal of Geophysical Research: Space Physics*, 125(4), e2019JA027750. doi:

580  
581  
582  
583  
584

10.1029/2019JA027750  
Zhao, L., Yu, Y., Delzanno, G. L., & Jordanova, V. K. (2015, 2020/08/25). Bounce-  
and mlt-averaged diffusion coefficients in a physics-based magnetic field geome-  
try obtained from ram-scb for the 17 march 2013 storm. *Journal of Geophysi-  
cal Research: Space Physics*, *120*(4), 2616–2630. doi: 10.1002/2014JA020858

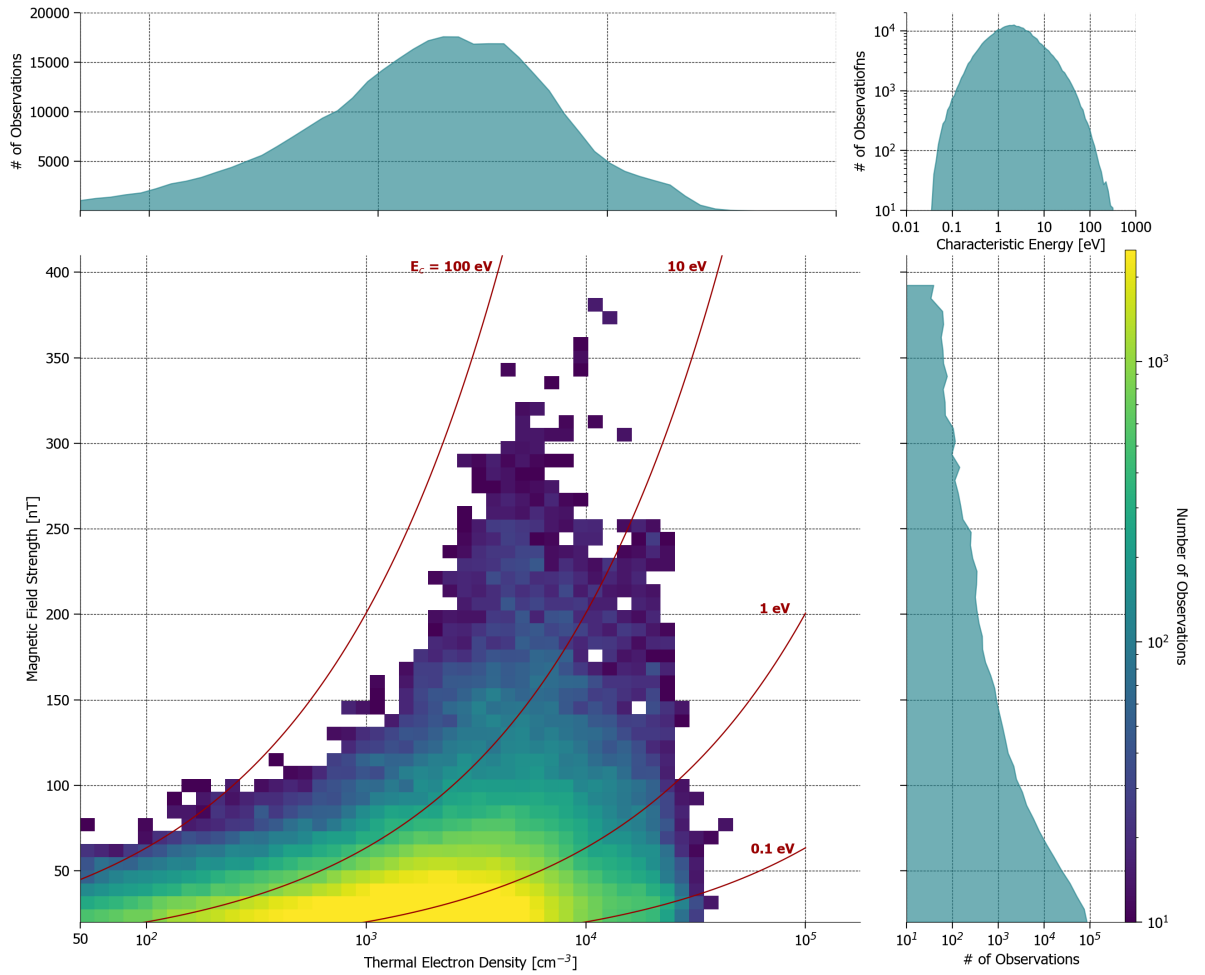


**Figure 1.** Histograms of the magnetic field strength and thermal electron density observed on dayside closed crustal fields at Mars. The color scale is logarithmic and ranges from 10 to 2500 observations. Bins with sample size  $< 10$  are not colored. Characteristic energy contours are shown in red. Histogram of the characteristic energy is shown in the upper right.

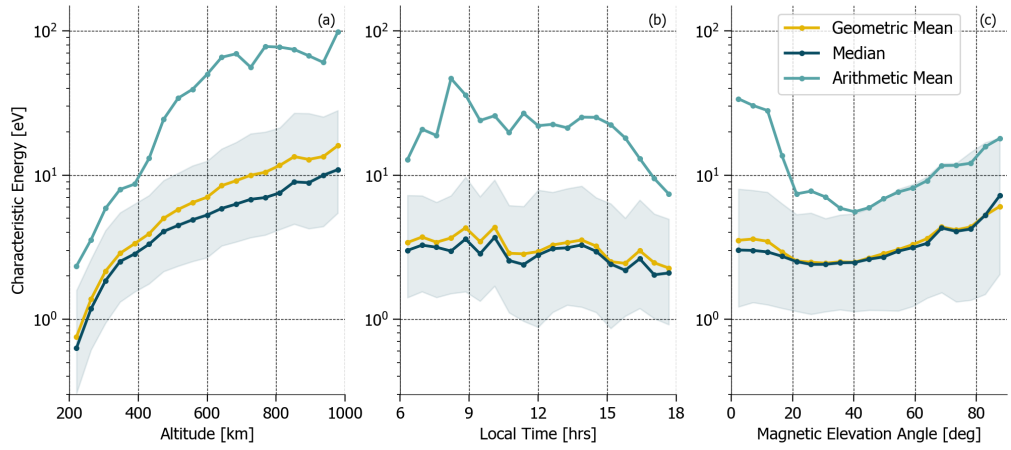


**Figure 2.** Characteristic energy distribution as a function of (a) altitude, (b) local time, and (c) magnetic elevation angle. The geometric mean, arithmetic mean, and median are all plotted and the region between the 25th and 75th percentiles is shaded.



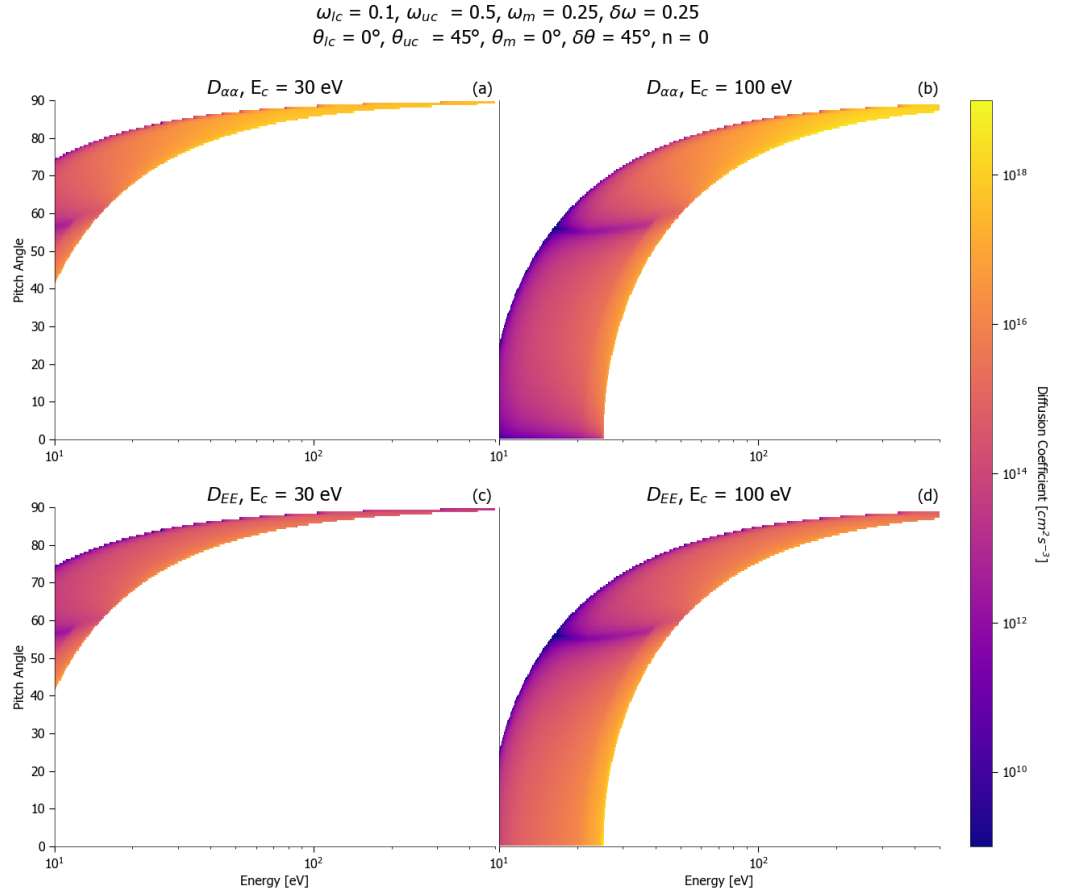


**Figure 3.** Pitch angle (top) and energy (bottom) diffusion coefficients for two characteristic energies: 30 eV (left) and 100 eV (right). The color scale is logarithmic and ranges 9 orders of magnitude. White regions indicate that no wave particle interaction occurs at that location in velocity space.

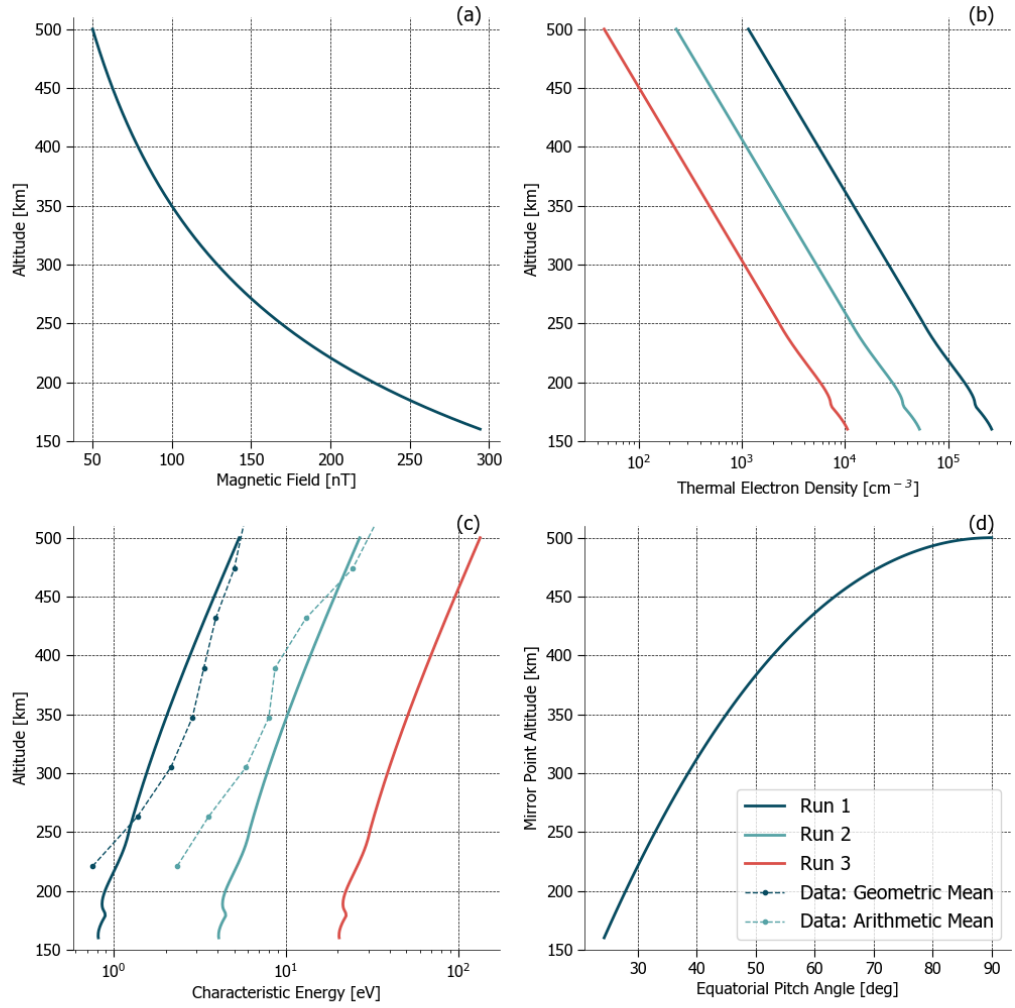


**Figure 4.** (a) Magnetic field strength of the dipole crustal field (b) Electron density profiles with a factor of 5 difference between Run 2 and Runs 1 & 3. (c) Characteristic energy altitude profile for each run (solid lines) and measured by MAVEN (dashed lines). (d) Mirror point altitude of electrons with varying equatorial pitch angles.

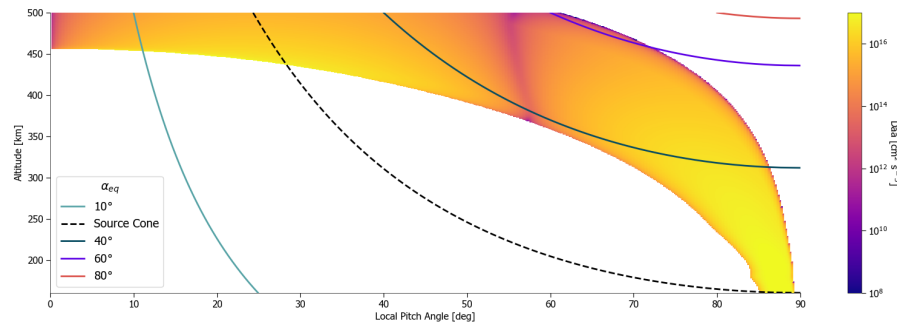


**Figure 5.** Trajectories of electrons with different equatorial pitch angles through altitude-pitch angle space for Run 3 conditions. The color depicts the magnitude of diffusion coefficients and maps the region where wave-particle interactions will occur with 25 eV electrons. The color scale is logarithmic and spans over 9 orders of magnitude. White regions indicate that resonance is not possible for 25 eV electrons at that local pitch angle and altitude

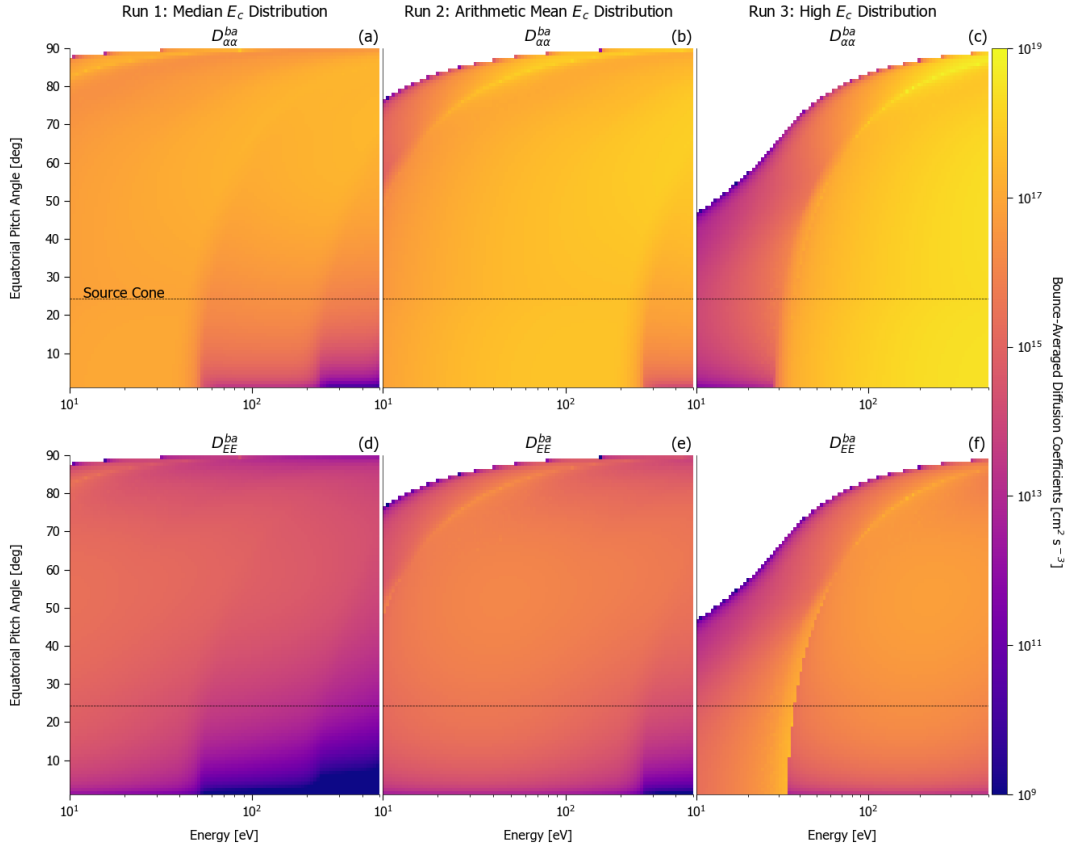


**Figure 6.** Bounce-averaged pitch angle (a, b, c) and energy (d, e, f) diffusion coefficients for Run 1 (a,d), Run 2 (b,e), and Run 3 (c,f). The black dashed line indicates the source cone pitch angle. The color scale is logarithmic and spans 10 orders of magnitude. White regions indicate equatorial plane velocity space regions where the electrons are not in resonance with the imposed waves.

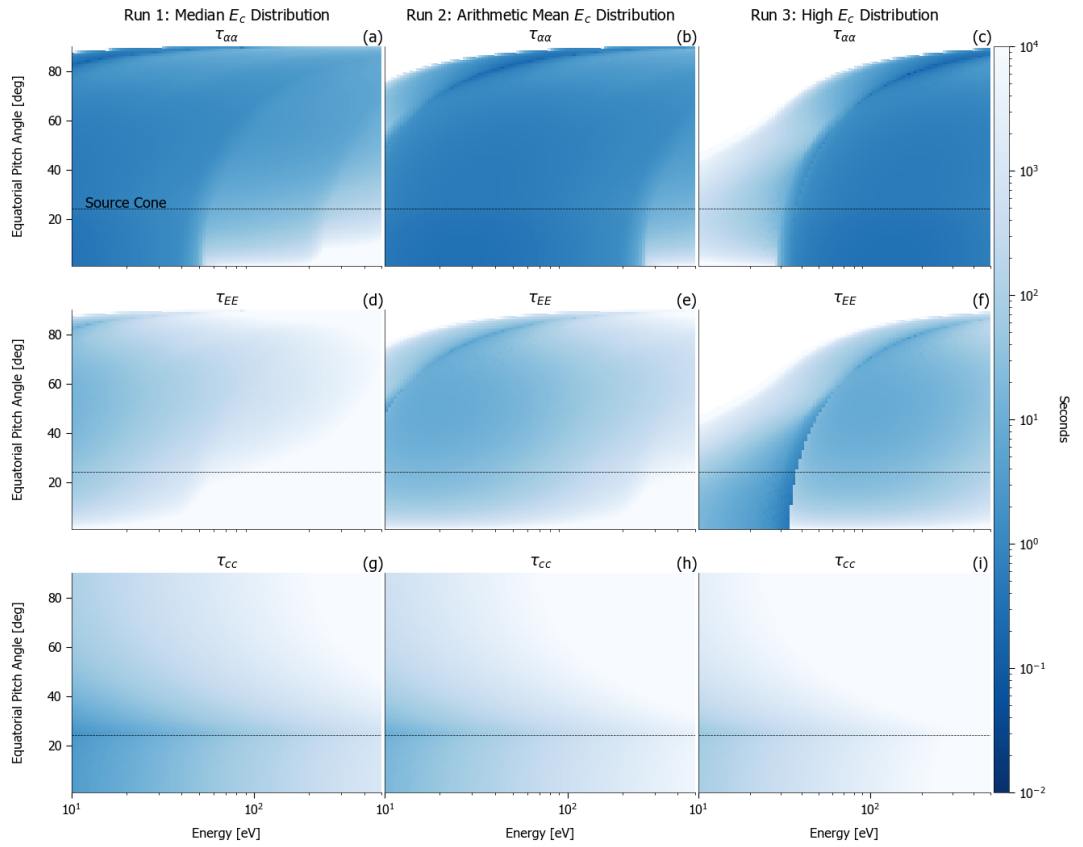


**Figure 7.** Time constants of interaction for pitch angle scattering (a, b, c), energization (d, e, f), and Coulomb collisions (g, h, i). The columns from left to right are for Runs 1, 2, and 3 respectively. The color scale is logarithmic and spans 6 orders of magnitude. The black dashed line indicates the source cone pitch angle.

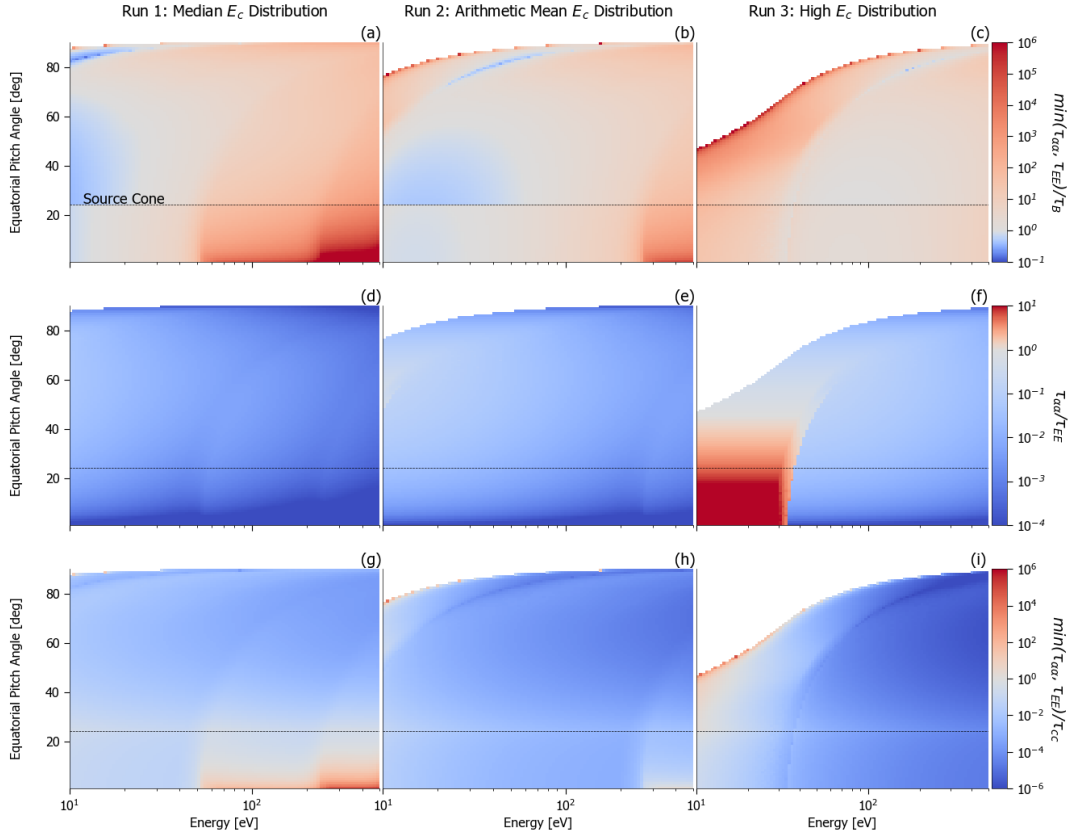


**Figure 8.** (a, b, c) Ratio of the fastest wave-particle interaction timescale to the electron bounce period. (d, e, f) Ratio of the pitch angle scattering timescale to energization timescale. (g, h, i) Ratio of the fastest wave-particle interaction timescale to the Coulomb collision timescale. The columns from left to right are for Runs 1, 2, and 3 respectively. The color scales are logarithmic and all diverge at a value of 1. The black dashed line indicates the source cone pitch angle. White regions indicate equatorial plane velocity space regions where the electrons are not in resonance with the imposed waves.

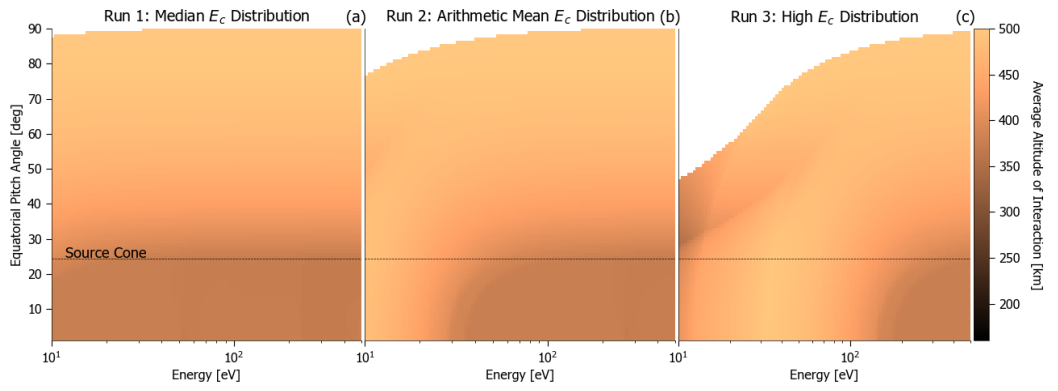


**Figure 9.** Average altitude of wave-particle interactions weighted by the base 10 logarithm of the local diffusion coefficients. The color scale is linear spanning a range of 350 km. White regions indicate equatorial plane velocity space regions where the electrons are not in resonance with the imposed waves. The black dashed line indicates the source cone pitch angle.